




Article

Computer-Assisted Detection of Cemento-Enamel Junction in Intraoral Ultrasonographs

Kim-Cuong T. Nguyen ^{1,2}, Yuening Yan ³, Neelambar R. Kaipatur ⁴, Paul W. Major ⁴, Edmond H. Lou ^{1,2,5}, Kumaradevan Punithakumar ^{1,*} and Lawrence H. Le ^{1,2,4,*}

¹ Department of Radiology and Diagnostic Imaging, University of Alberta, Edmonton, AB T6G 2B7, Canada; cuong1@ualberta.ca

² Department of Biomedical Engineering, University of Alberta, Edmonton, AB T6G 2V2, Canada

³ Institute of Neuroscience and Psychology, University of Glasgow, Glasgow G12 8QQ, UK; y.yan.2@research.gla.ac.uk

⁴ School of Dentistry, University of Alberta, Edmonton, AB T6G 1C9, Canada; kaipatur@ualberta.ca (N.R.K.); major@ualberta.ca (P.W.M.)

⁵ Department of Electrical and Computer Engineering, University of Alberta, Edmonton, AB T6G 1H9, Canada; elou@ualberta.ca

* Correspondence: punithak@ualberta.ca (K.P.); lawrence.le@ualberta.ca (L.H.L.)

Featured Application: To detect the cemento-enamel junction (CEJ) in B-mode intraoral ultrasound images for periodontal diagnosis and orthodontic treatment planning.



Citation: Nguyen, K.-C.T.; Yan, Y.; Kaipatur, N.R.; Major, P.W.; Lou, E.H.; Punithakumar, K.; Le, L.H. Computer-Assisted Detection of Cemento-Enamel Junction in Intraoral Ultrasonographs. *Appl. Sci.* **2021**, *11*, 5850. <https://doi.org/10.3390/app11135850>

Academic Editor:
Davide Fontanarosa

Received: 14 May 2021
Accepted: 17 June 2021
Published: 23 June 2021

Publisher's Note: MDPI stays neutral with regard to jurisdictional claims in published maps and institutional affiliations.



Copyright: © 2021 by the authors. Licensee MDPI, Basel, Switzerland. This article is an open access article distributed under the terms and conditions of the Creative Commons Attribution (CC BY) license (<https://creativecommons.org/licenses/by/4.0/>).

Abstract: The cemento-enamel junction (CEJ) is an important reference point for various clinical measurements in oral health assessment. Identifying CEJ in ultrasound images is a challenging task for dentists. In this study, a computer-assisted detection method is proposed to identify the CEJ in ultrasound images, based on the curvature change of the junction outlining the upper edge of the enamel and cementum at the cementum–enamel intersection. The technique consists of image preprocessing steps for image enhancement, segmentation, and edge detection to locate the boundary of the enamel and cementum. The effects of the image preprocessing and the sizes of the bounding boxes enclosing the CEJ were studied. For validation, the algorithm was applied to 120 images acquired from human volunteers. The mean difference of the best performance between the proposed method and the two raters' measurements was an average of 0.25 mm with reliability ≥ 0.98 . The proposed method has the potential to assist dental professionals in CEJ identification on ultrasonographs to provide better patient care.

Keywords: high-frequency ultrasound; landmark detection; dento-periodontium; cemento-enamel junction; oral health; image processing

1. Introduction

Periodontitis or periodontal (gum) disease is one of the most common oral diseases, affecting 20–50% of the population globally [1]. Periodontitis can result in eventual tooth loss as a consequence of gradual weakening and loss of the tooth-supporting periodontium. Aggressive periodontitis, characterized by an early onset rapid progression of destruction, is more common in children and adolescents. Diagnosis of periodontitis is based on clinical signs and symptoms such as gingival recession, bleeding on probing, increased pocket depth, clinical attachment loss, alveolar bone loss, and root resorption [2].

The cemento-enamel junction (CEJ) or cervical line is a line on the tooth's surface where the cementum on the root meets the enamel on the crown. The CEJ is considered one of the most relevant landmarks to diagnose periodontal disease and its distance to other reference points such as gingival margin, alveolar bone crest, or furcation entrance is used to evaluate gingival recession, clinical attachment loss [3,4], alveolar bone loss [5–7],

or furcation involvement [8]. Thus, CEJ identification to diagnose periodontal disease and design an orthodontic treatment plan is paramount for clinical success.

In clinical practice, several methods have been used to locate CEJ. A common approach is the visual localization method, in situations where the CEJ is coronal to the gingival margin. Most often, CEJ is covered by the gingival tissue and is apical to the gingival margin; hence, a tactile method using a periodontal probe is the preferred approach [4]. Occasionally, probe sensitivity can erroneously identify root surface irregularities as CEJ.

In contrast to probing, radiography allows for noninvasive imaging of the CEJ and alveolar bone crest with no errors in identification caused by inflamed gingival tissues [5–7,9]. The work of Pecoraro and his colleagues showed accuracy in alveolar bone height measurements using digital radiography in comparison to the conventional method in measuring the CEJ–bone crest distance [6]. Although the reported absolute differences between the two examiners were significant, the standard deviation was less than 1 mm, which was acceptable when compared with measurements obtained using a 1-mm graduated periodontal probe. Intraoral 2D periapical radiographs are useful for identifying CEJ and alveolar bone in the interproximal areas. However, overlapping of 3D anatomic structures prevents accurate visualization of CEJ and bone crest on the buccal (cheek) or lingual/palatal (tongue) side of the teeth. Computer-assisted detection of CEJ in 2D digital dental radiographs was reported in early 1989, with the same limitations as film radiographic images in the identification of CEJ [10].

Cone beam computed tomography (CBCT), which is an X-ray-based imaging technique, generates 3D volumetric image reconstruction and visualization of internal anatomical features [11,12]. In comparison with 2D radiography, CBCT has much better accuracy and resolution due to the absence of overlapping tissues, but it exposes the patient to a much higher radiation dose [13]. Therefore, CBCT is not recommended for routine use in young growing patients or repeated imaging.

The applications and development of ultrasound in dentistry, especially in periodontics, have been extensively reported [14–23]. Ultrasound is a noninvasive, ionizing-radiation-free, economical, and portable diagnostic tool for hard and soft tissue imaging. A high correlation in alveolar bone level (CEJ—alveolar bone crest) was demonstrated between ultrasound and microscopy ($R = 0.79$) and between ultrasound and CBCT ($R = 0.98$) [15,19]. Chan's study also showed a high correlation in measuring the facial crestal bone level (CEJ—alveolar bone crest) between ultrasound and CBCT ($R = 0.78$) or direct measurement ($R = 0.88$) [16]. However, identifying CEJ in ultrasound images demands clinicians to have extensive knowledge and experience in ultrasound and scanning operations, which is deemed difficult as the imaging modality is new in the field of dentistry. In addition, ultrasound images contain the multiplicative speckle or granular noises caused by backscatters from small inhomogeneities in the target tissue as well as salt and pepper noises by the device. Their inherent existence greatly lowers the signal-to-noise ratio and degrades the image quality [24]. Noise removal methods such as spatial averaging [25], homomorphic filtering [26], Weiner filtering [25], adaptive median filtering [24], and soft-thresholding techniques [27] have been studied to filter out noises and enhance signals.

The objective of this study is to develop a computer-assisted method for detecting CEJ in B-mode intraoral ultrasound images and to evaluate the efficacy of the proposed method. A combination of homomorphic filtering, contrast enhancement, and adaptive median filtering was used to reduce the effects of speckle noise and enhance the structures of interest.

2. Materials and Methods

2.1. Data Collection

Forty incisors from fifteen adolescent volunteers (aged 12–17 years) and one adult volunteer (25 years old from the author's (LHL) research laboratory) were scanned at Kaye Edmonton dental clinic, University of Alberta with University ethics approval (Pro00062355).

Ultrasound scanning was performed at 20 MHz using a SonixTablet portable medical ultrasonic system (Analogic, Vancouver, BC, Canada) and a linear phased array transducer (L40-8/12, Analogic, Vancouver, Canada). The long axis of the transducer was positioned on a piece of 5 mm-thick gelatin-based gel pad located on the labial side of the tooth and gingiva in alignment with the longitudinal axis of the tooth [21]. The gel pad also functioned to ensure the region of interest (ROI) within the focal zone of the ultrasound beam for optimum resolution. Three different ultrasound images were selected for each tooth to make up a data set of 120 images for this study.

2.2. Image Preprocessing

Figure 1 illustrates the components of the proposed process to identify CEJ including the image preprocessing.

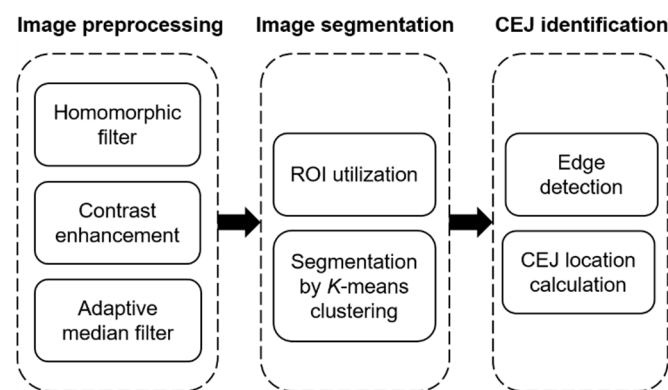


Figure 1. The image preprocessing and detection processes of the proposed method to identify CEJ.

2.2.1. Homomorphic Filtering

In this study, a 2D ultrasound image $d(i, j)$ is a matrix of pixels with intensity, where i is the index along the horizontal direction parallel to the long axis of the transducer and j is the index along the depth axis perpendicular to the transducer surface. Homomorphic filtering was used to remove speckle multiplicative noises by breaking up the multiplicative noise into additive noise. Recently, it was used to denoise the ultrasound images from porcine samples prior to segmentation of alveolar bone [18]. The filter consists of five stages as indicated in Figure 2 [20] where $\hat{d}(i, j)$ is the filtered image. The homomorphic filtering balances the illuminance of the image by reducing the effect of the dominant intensities while enhancing the contribution of the low intensities so that the low-intensity features can be visible. The reflectance of features such as interfaces, characterized by high frequencies, can also be sharpened. Following [28] closely, the transfer function of the filter is

$$H(u, v) = (\gamma_H - \gamma_L) \left\{ 1 - \exp \left[-c \left(\frac{D(u, v)}{D_o} \right)^2 \right] \right\} + \gamma_L, \quad (1)$$

where γ_H and γ_L are the high and low frequency gains, respectively; D_o is the cut-off frequency; c is a constant that controls the steepness of the slope of the function between γ_H and γ_L ; and $D(u, v)$ is the distance between a point (u, v) and the center of the $P \times Q$ frequency map, i.e.,

$$D(u, v) = [(u - P/2)^2 + (v - Q/2)^2]^{1/2}, \quad (2)$$

where P and Q are the padded size.

2.2.2. Contrast Enhancement

Due to the inherent properties of ultrasound imaging, the selected ROI had low contrast. Therefore, a linear contrast enhancement approach was utilized to enhance the contrast of the images by expanding the original image intensity values linearly, which

improved the detection of the tissue boundary [20]. The image contrast enhancement was achieved by linearly scaling the histogram. It mapped the pixel intensities $\hat{d}(i,j)$'s to new values such that 1% of the data was saturated at low and high intensities, which aided in distinguishing the structures of enamel and cementum from other blurred areas.

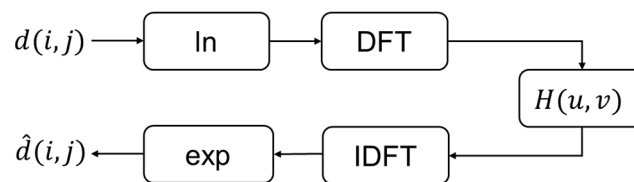


Figure 2. Homomorphic filtering. The input $d(i,j)$ and the output $\hat{d}(i,j)$ are the unprocessed and filtered images, respectively. The components include logarithmic transformation (ln), 2D discrete Fourier transform (DFT), Gaussian high-pass filtering $[H(\cdot)]$, 2D inverse discrete Fourier transform (IDFT), and exponential transformation (exp).

2.2.3. Adaptive Median Filtering

The adaptive median filter is a nonlinear filter that outputs the median value of the input samples of an array. The array size was 7×7 in this study. Median filtering is very effective at removing spurious or “salt and pepper” noise [29].

2.3. Image Segmentation

To obtain an accurate and repeatable detection of the CEJ location, an initial ROI consisting of the CEJ and a portion of the enamel and cementum was manually selected and extracted for further analysis. We chose the ROI as a rectangular bounding box. Since the box size or shape was determined to include features such as alveolar bone and exclude features such as enamel and gingiva as much as possible, the aspect ratio could be varied. In practice, the clinician can select the aspect ratio to suit the problem at hand. *K*-means clustering was used to identify the foreground and background regions within the initial ROI. The *K*-means ($K = 2$) was used to set two preclassified labels and build the initial graph. The proposed *K*-means approach partitioned pixel intensities into two initial clusters based on their similarity to the clustering centers [30]. The centers were automatically adjusted based on the average intensity of pixels in each cluster. This step was repeated until convergence, where the average values were no longer changing.

2.4. CEJ Selection

After the bounding box was selected, the algorithm extracted every point in the foreground region and detected the edge corresponding to the upper border of the enamel–cementum region. Since enamel and cementum are strong ultrasound reflectors, their intensities are very large in comparison with those of gingiva [17]. The contour of the tooth has a small V-shaped valley at the neck of the tooth where the enamel and cementum meet [31]. The bottom of the valley is the location of the CEJ. Based on these characteristics, the detection algorithm calculated the absolute value of the vertical change, Δj , of the two consecutive pixels along the detected enamel–cementum border, and then compared the value with that of the previous location. The position of the CEJ was determined by the location with the greatest absolute change $|\Delta j|_{max}$. Finally, remapping the coordinate of the CEJ back to its original coordinate, the algorithm marked the CEJ in the original image.

The algorithm was implemented on a 64-bit Windows 10 operating system with an Intel Core i5-2500 Quad-Core (3.30 GHz) CPU and 8 GB random access memory (RAM). The image processing and CEJ detection were realized through MATLAB version R2020b (MathWorks, Natick, MA, USA). Our user interface allows the user to select the images directly from the monitor’s screen with the option to manually select the CEJ location or to detect it using the proposed detection method.

2.5. Validation

The CEJ detection results by the proposed method were validated by comparing the detected CEJ locations with the manually labeled ground truth by two raters. Raters R1 (a biomedical engineer) and R2 (an experienced orthodontist) have about 8 years and 2 years of experience with dental ultrasound, and 10 years and 20 years of experience in their field, respectively. To evaluate the intrarater reliability, each rater performed the measurements twice with one week apart to avoid bias.

The impact of image preprocessing including homomorphic filtering, adaptive median filtering, and contrast enhancement was investigated. We also examined the effect of the bounding box size on the accuracy of the method by comparing three sizes: small (SBB, 31×41 pixels), medium (MBB, 51×71 pixels), and large (LBB, 81×101 pixels) with the same center pixel (Figure 3). For example, 31×41 pixels, 51×71 pixels, and 81×101 pixels correspond to 1.4 mm^2 , 3.9 mm^2 , and 8.9 mm^2 respectively. Therefore, the areas of MBB and LBB were approximately 3 and 6 times of SBB's area, respectively.

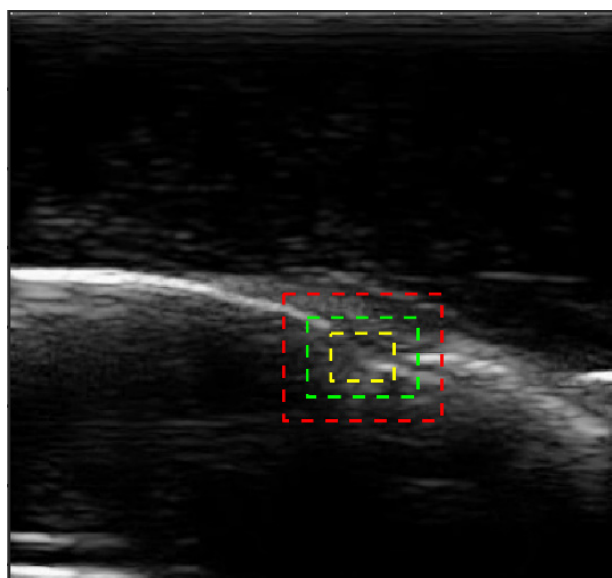


Figure 3. An example shows three different bounding box sizes: SBB in yellow, MBB in green, and LBB in red in the same image.

The locations of the CEJ identified by the proposed method for the three bounding boxes with and without image preprocessing scenarios were compared with the two raters' labels. The discrepancies or differences in locating the CEJ between the proposed method and each rater for 120 ultrasound images were measured in Euclidean distances. A descriptive analysis was performed using the mean difference (MD), standard deviation (SD), and box plots. The intraclass correlation coefficients (ICC) were calculated to assess the intrarater, interrater, and intermethod reliabilities based on a single-rating ($k = 1$), absolute-agreement, and 2-way mixed-effects model. ICC values < 0.5 , between 0.5 and 0.75, between 0.75 and 0.9, and > 0.90 are indicative of poor reliability, moderate reliability, good reliability, and excellent reliability, respectively [32]. A two-tailed power analysis was performed to determine the sample size using the following parameters: minimum acceptable reliability = 0.90, expected reliability = 0.95, significance level = 0.05, and power = 80%.

3. Results

A schematic of the tooth and normal periodontium showing the V-shaped identification of the CEJ was illustrated in Figure 4a. The ultrasound images before and after image preprocessing are shown in Figure 4b,c. The homomorphic filtering with a Gaussian filter removed multiplicative noise significantly and sharpened features of the image. By

enhancing contrast, the structures of enamel and cementum become much sharper and are clearly distinguishable from other regions. Adaptive median filtering suppressed subtle speckle noise while preserving edge detail. Compared to the original image, the preprocessing improved the clarity of the images, making the following extraction more reliable and tenable. The average computational time for the preprocessing steps was 0.09 s for each image.

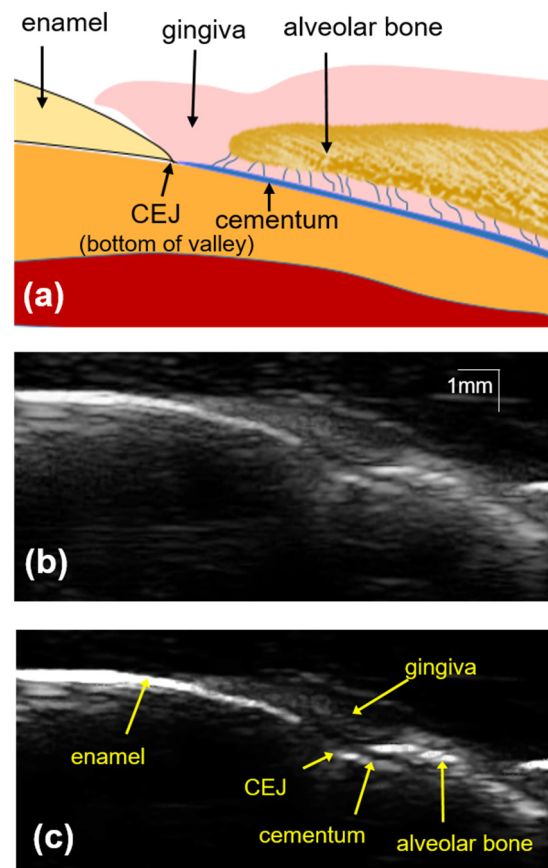


Figure 4. (a) A schematic cross-section of a tooth and its periodontium; (b) the in vivo intraoral ultrasound images before image processing; (c) the processed image after homomorphic filtering, contrast enhancement, and adaptive median filtering.

Figure 5 illustrates the segmentation and CEJ detection by the proposed method. The algorithm initially required a bounding box (81×101 pixels in this example) containing the CEJ (Figure 5a). Then, the image was classified into several areas based on the gray-level values. Figure 5b presents a color plot of the ROI where the high-intensity areas correspond to the enamel, cementum, or bone structures. Finally, *K*-means clustering accurately extracted the two clusters of interest while rejecting other areas, resulting in a binary map where the hard tissues (enamel or bone) are indicated in black (Figure 5c). It took approximately 0.69 s for the segmentation on average. Figure 5d shows a curve joining the upper borders of the identified pixels of the extracted region. The numerical differential between adjacent pixels along the curve was estimated (Figure 5e), and the CEJ was determined at the position of the maximum absolute of the differential (Figure 5f). The average time of the CEJ detection process was 0.27 s. The total time for the CEJ prediction including preprocessing steps was 1.05 s. The identified position was then incorporated into the image as a red dot (Figure 5g).

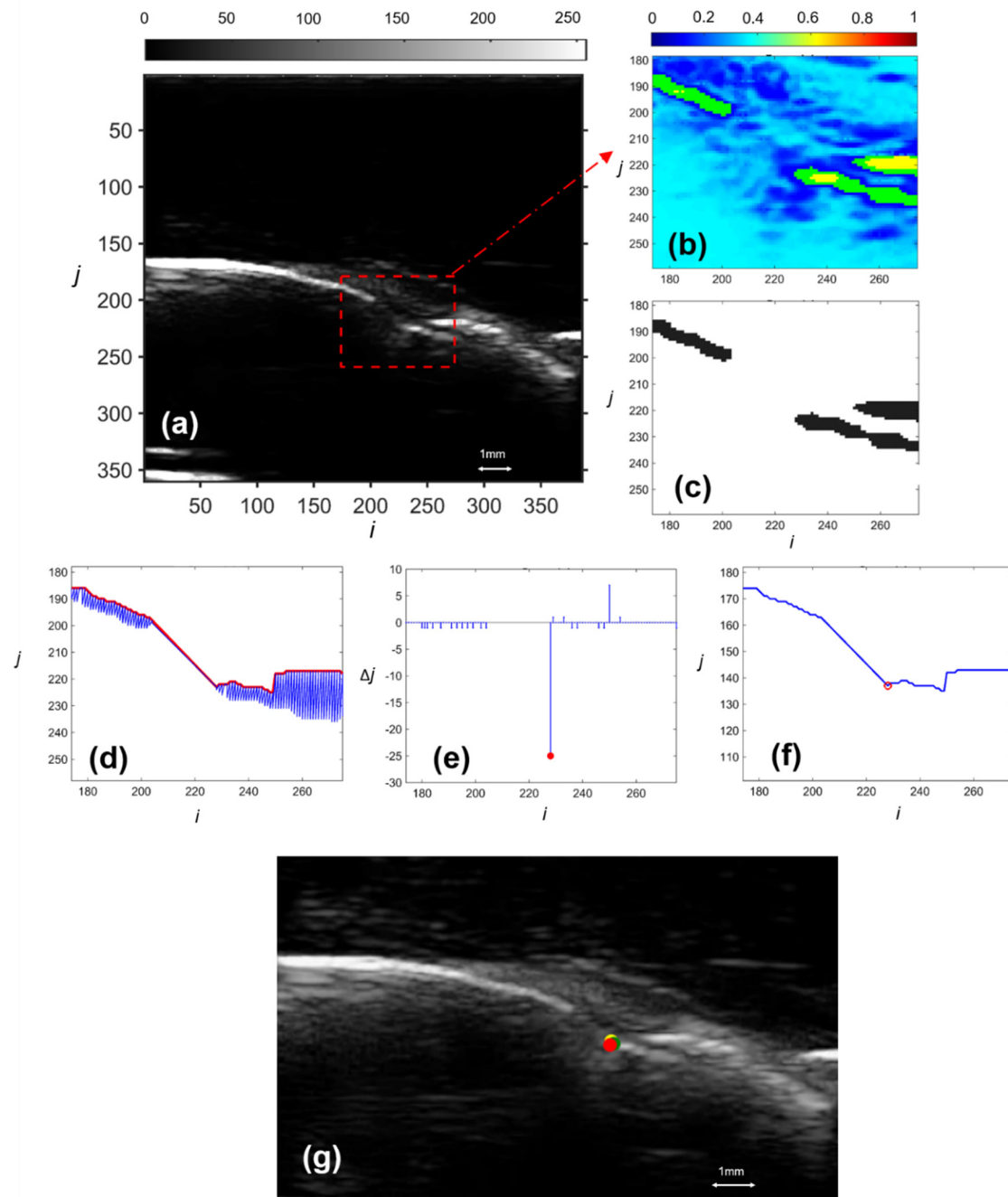


Figure 5. An example of the computer-assisted CEJ detection on an ultrasound image. (a) A bounding box containing the CEJ; (b) the corresponding color image of the ROI; (c) region extraction using *K*-mean clustering; (d) edge detection; (e) local difference calculation; (f) CEJ identification at maximum difference; (g) comparison of the CEJ location by the proposed method (red dot) and manual CEJ identification by raters 1 and 2 (green and yellow dots).

Table 1 summarizes the CEJ detection results between two manual labels by the same rater (intrarater), between two raters (interrater), and the difference between raters and the method (intermethod) with and without image preprocessing and for three bounding box sizes, i.e., small (SBB), medium (MBB), large (LBB). The two scenarios are with all three image preprocessing steps (A or proposed method) and without image preprocessing steps (B). The clinical tolerance limit of 0.5 mm based on direct probing measurements was used as a reference [33]. The MDs \pm SDs of the mismatches vary from 0.21 ± 0.24 mm to 0.31 ± 0.32 mm for the intrarater and around 0.23 ± 0.24 mm for the interrater. The average ICC values and percentages of images that have less than 0.5 mm mismatch between the

proposed method and two raters were 0.990 and 96%; 0.985 and 92%; and 0.982 and 90% for SBB, MBB, and LBB, respectively. These values were close to the interrater (93%) and higher than the intrarater average (88%). The results without image preprocessing (B) provide higher MD (average 0.32–0.55 mm), lower ICC values (average 0.943–0.983), and a smaller percentage of images with <0.5 mm difference (average 55–85%) in comparison with image preprocessing (A) for all three box sizes. The mean differences between the two raters and the proposed method (A) increase slightly on average from 0.25 mm to 0.30 mm with the increase of the bounding box size. The distributions of the differences between the proposed method and raters 1 and 2 are also displayed in the box plots (Figure 6). The data dispersion, measured by the interquartile range (IQR), covers 50% of the data points [34]. The IQRs are small or tight for scenarios A for all box sizes and within the 0.5 mm clinical limit.

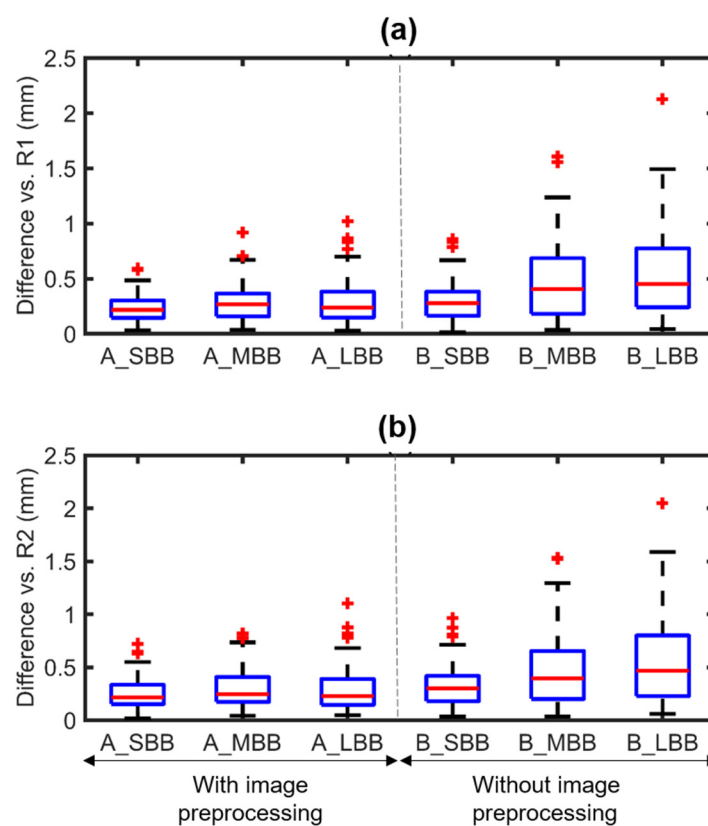


Figure 6. Box plots show the difference between the proposed method and rater 1 (a) or rater 2 (b) for different bounding box sizes (SBB, MBB, LBB) and two scenarios (A) with image preprocessing and (B) without image preprocessing. The red line in each box denotes the median value; the top and bottom hinges of the box correspond to the 25th (Q1) and 75th (Q3) percentiles, respectively. The interquartile range (IQR) is given by the interval bounded by Q1 and Q3. The minimum ($Q1 - 1.5 \times IQR$) and maximum ($Q3 + 1.5 \times IQR$) limits (indicated by horizontal bars) are linked to the hinges using whiskers. Data points outside these extreme values are considered potential outliers, which are indicated by the red plus signs.

Table 1. Comparison of CEJ identification between the proposed method and the two raters for different bounding box sizes (SBB, MBB, LBB) with image preprocessing scenarios (A) and without (B). The full size refers to the whole image size (e.g., 360×386 pixels). SBB, MBB, and LBB denote the small (31×41 pixels), medium (51×71 pixels), and large (81×101 pixels) bounding boxes, respectively.

| | | MD (mm) | SD (mm) | ICC | Images with Difference < 0.5 mm (%) |
|----------------------------|---------|------------|------------|---------------------|--|
| Full size | R11–R12 | 0.21 | 0.24 | 0.983 [0.978,0.987] | 90 |
| | R21–R22 | 0.31 | 0.32 | 0.969 [0.960,0.978] | 85 |
| | R1–R2 | 0.23 | 0.24 | 0.983 [0.979,0.987] | 93 |
| SBB 31 × 41 (pixel) | R1–A | 0.23 | 0.12 | 0.991 [0.989,0.993] | 98 |
| | R2–A | 0.26 | 0.15 | 0.988 [0.984,0.991] | 94 |
| | R1–B | 0.30 | 0.20 | 0.985 [0.980,0.988] | 87 |
| | R2–B | 0.33 | 0.19 | 0.980 [0.974,0.985] | 83 |
| MBB 51 × 71 (pixel) | R1–A | 0.28 | 0.16 | 0.985 [0.981,0.989] | 92 |
| | R2–A | 0.30 | 0.17 | 0.984 [0.979,0.987] | 91 |
| | R1–B | 0.46 | 0.33 | 0.959 [0.948,0.968] | 62 |
| | R2–B | 0.47 | 0.33 | 0.957 [0.945,0.967] | 63 |
| LBB 81 × 101 (pixel) | R1–A | 0.29 | 0.18 | 0.983 [0.978,0.986] | 90 |
| | R2–A | 0.30 | 0.20 | 0.981 [0.976,0.985] | 89 |
| | R1–B | 0.54 | 0.38 | 0.944 [0.928,0.956] | 57 |
| | R2–B | 0.56 | 0.38 | 0.941 [0.924,0.954] | 53 |

4. Discussion

Innovations in medical imaging have helped mankind to achieve an enhanced quality of life. Although X-rays have been the mainstay in medical imaging, the concern about the harmful effects of ionizing radiation, especially for pediatric and adolescent patients due to its frequent use in medicine and dentistry, is ever-growing. Current research has been focused on developing new modalities such as ultrasound and magnetic resonance for medical and dental imaging. Ultrasound uses compressional waves to image the internal structures of the tissues. The ultrasound technique has numerous benefits which include portability, cost savings, and especially safety for not using ionizing radiation. This imaging modality has the advantage of being able to measure the thickness and elasticity of the gingiva, which is deemed difficult with conventional radiographic imaging modalities. Beyond these advantages, ultrasound imaging has some drawbacks. The images lack resolution and contrast. The signal-to-noise ratio is low with speckle noise. Furthermore, interpreting the ultrasound images is challenging due to the interference of wave propagation characteristics. Increasing the frequency to enhance the resolution for fine details can be investigated, but the depth penetration becomes limited, and more ultrasound scattering is expected to deteriorate the image quality.

CEJ is considered an important reference landmark for various clinical measurements in oral health assessment, such as gingival attachment level and alveolar bone crest level. Since CEJ is stable over time, it provides an excellent reference for evaluating disease progression and treatment intervention. The challenge of accurately localizing the CEJ is not only limited by errors in the measurement systems, but is compounded by the fact that the enamel and cementum boundaries are irregular, and their curvatures vary among different teeth. Based on the gradual thinning characteristics of the enamel toward the cementum, the ultrasound response shows a valley in the B-mode image with a low corresponding to the position of CEJ, and a detection method is proposed in this study to locate CEJ in ultrasound images.

The proposed technique includes image processing steps prior to CEJ detection to minimize the multiplicative speckle noise and impulsive noise by homomorphic filtering

and adaptive median filtering. Using 120 intraoral ultrasound images from human volunteers as validation samples, the evaluation showed that the proposed method had high conformance with the raters within the clinical limit. The validation result suggests that the MDs of the intermethod (between the proposed method and the raters) were not much different from the manual interrater and intrarater mismatches, i.e., 0.23–0.30 mm versus 0.21–0.31 mm. The average intrarater reliabilities (ICC = 0.976) and interrater reliability (ICC = 0.983) are smaller than the reliabilities between the proposed method and two raters for all small (ICC = 0.990) and medium (ICC = 0.985) bounding box sizes. The MD increases and the reliability decreases with the box size. In practice, the box size is determined by including the anatomical structures of interest in the ultrasound image. The results also showed the contribution of image preprocessing steps in the improvement of the proposed method. The bigger the bounding box, the more likely the additional irrelevant low and high frequency (isolated) structures will be included, which might affect the identification result. Our results have shown that image preprocessing played a role in reducing the impact of those structures, which are prominent in the larger bounding box. The proposed image processing would be quite beneficial for novice clinicians who tend to choose a larger region of interest corresponding to a larger box. The proposed method took around a second to identify the CEJ, much faster than manual human visualization and interpretation.

Previous studies have reported visualization improvements with the segmentation of ultrasound images, including soft tissue [35] and cortical bone [36]. In dentistry, computer-assisted methods have been studied to identify the dental structures in ultrasound images such as gingival sulcus [37] and alveolar bone [20,21,38]. However, previous research did not focus on CEJ detection. Dental clinicians are not typically trained in ultrasound image interpretation. Therefore, this algorithm may assist clinicians in identifying CEJ in ultrasound images automatically with limited training. The location of the CEJ is difficult to detect due to the low contrast-to-noise ratio of the ultrasound images. The proposed method could provide a reference check to clarify the ambiguous situation and increase efficiency and productivity.

The findings of this study are subject to several limitations. First, this study focused on using ultrasound images of the incisor teeth. This is due to the fact that the size of the transducer restricts its reach intraorally. Research using more ultrasound images of canine, molar, and premolar teeth in other parts of the oral cavity should be performed to further validate the method. Second, though the method has been demonstrated to be feasible, the manual selection of the bounding box depends on the subjective expertise of the examiner, which, in turn, would induce a considerable degree of examiner-dependent bias. Third, this is preliminary work with a small sample size for feasibility. Recent developments in machine learning offer options to automatically select the bounding box, which eliminates subjective bias and can strengthen the validity of our current method [39,40]. For the first time, the application of machine learning algorithms to detect alveolar bones in ultrasound images was reported by our research group [21,38]. Deep learning techniques with a very large database to train the convolution neural networks for CEJ detection should be explored in future research.

5. Conclusions

CEJ is an important landmark, and accurate identification of the CEJ location from diagnostic images is important for oral clinicians. This study presents a computer-assisted detection method to identify CEJ in ultrasound images, utilizing the characteristic response of CEJ in B-mode ultrasound images. Using 120 in vivo human ultrasound images, the proposed method demonstrated that the computer-assisted detection of CEJ is reasonably accurate for clinical applications.

Author Contributions: Conceptualization, K.-C.T.N., P.W.M., L.H.L. and N.R.K.; methodology, K.-C.T.N., Y.Y., N.R.K., K.P., E.H.L. and L.H.L.; software, K.-C.T.N., Y.Y. and K.P.; validation, K.-C.T.N., Y.Y. and N.R.K.; formal analysis, K.-C.T.N. and Y.Y.; investigation, L.H.L. and K.P.; resources,

E.H.L., L.H.L., N.R.K. and P.W.M.; data curation, K.-C.T.N., Y.Y. and N.R.K.; writing—original draft preparation, K.-C.T.N., Y.Y., N.R.K., K.P. and L.H.L.; writing—review and editing, K.-C.T.N., Y.Y., N.R.K., E.H.L., L.H.L., K.P. and P.W.M.; visualization, K.-C.T.N., Y.Y., K.P. and L.H.L., supervision, P.W.M., L.H.L. and K.P.; project administration, K.-C.T.N., K.P. and L.H.L.; funding acquisition, L.H.L. and P.W.M. All authors have read and agreed to the published version of the manuscript.

Funding: This research has been funded by the generous support of the Stollery Children’s Hospital Foundation through the Women and Children’s Health Research Institute. The authors would like to acknowledge the support from the Natural Sciences and Engineering Research Council of Canada (NSERC), Alberta Innovates Technology Futures Graduate studentship, MITACS and Chinese Scholarship Council internship.

Institutional Review Board Statement: The study was carried out successfully under the approval by the University Research Ethics Office (HRED No: Pro00062355).

Informed Consent Statement: Informed consent was obtained from all subjects involved in the study.

Data Availability Statement: Data available on request due to privacy or ethical restrictions.

Acknowledgments: The authors thank Susan Helwig, Manuel Lagravere Vich, and Tarek El-Bialy, School of Dentistry—Kaye Edmonton Clinic, for their assistance in acquiring the ultrasound data.

Conflicts of Interest: The authors declare no conflict of interest. The funders had no role in the design of the study; in the collection, analyses, or interpretation of data; in the writing of the manuscript, or in the decision to publish the results.

References

1. Sanz, M.; D’Aiuto, F.; Deanfield, J.; Fernandez-Avilés, F. European workshop in periodontal health and cardiovascular disease—scientific evidence on the association between periodontal and cardiovascular diseases: A review of the literature. *Eur. Heart J. Suppl.* **2010**, *12*, B3–B12. [[CrossRef](#)]
2. Dentino, A.; Lee, S.; Mailhot, J.; Hefti, A.F. Principles of periodontology. *Periodontol.* **2000**, *2013*, *61*, 16–53. [[CrossRef](#)]
3. Charalampakis, G.; Dahlén, G.; Carlén, A.; Leonhardt, Å. Bacterial markers vs. clinical markers to predict progression of chronic periodontitis: A 2-yr prospective observational study. *Eur. J. Oral Sci.* **2013**, *121*, 394–402. [[CrossRef](#)] [[PubMed](#)]
4. Khaw, A.; Liberali, S.; Logan, R.; Keefe, D.; Bartold, P.M. Influence of periodontitis on the experience of oral mucositis in cancer patients undergoing head and neck radiotherapy: A pilot study. *Support. Care Cancer* **2014**, *22*, 2119–2125. [[CrossRef](#)]
5. Cairo, F.; Carnevale, G.; Nieri, M.; Mervelt, J.; Cincinelli, S.; Martinolli, C.; Pini-Prato, G.P.; Tonetti, M.S. Benefits of fibre retention osseous resective surgery in the treatment of shallow infrabony defects. A double-blind, randomized, clinical trial describing clinical, radiographic and patient-reported outcomes. *J. Clin. Periodontol.* **2013**, *40*, 163–171. [[CrossRef](#)]
6. Pecoraro, M.; Azadivatan-Le, N.; Janal, M.; Khocht, A. Comparison of observer reliability in assessing alveolar bone height on direct digital and conventional radiographs. *Dentomaxillofac. Radiol.* **2005**, *34*, 279–284. [[CrossRef](#)] [[PubMed](#)]
7. Hou, G.-L.; Hung, C.-C.; Yang, Y.-S.; Shieh, T.-Y.; Tsai, C.-C. Radiographic alveolar bone loss in untreated Taiwan Chinese subjects with adult periodontitis measured by the digital scanning radiographic image analysis method. *Dentomaxillofac. Radiol.* **2003**, *32*, 104–108. [[CrossRef](#)] [[PubMed](#)]
8. Wang, H.-L.; Burgett, F.G.; Shyr, Y.; Ramfjord, S. The Influence of Molar Furcation Involvement and Mobility on Future Clinical Periodontal Attachment Loss. *J. Periodontol.* **1994**, *65*, 25–29. [[CrossRef](#)]
9. Tihanyi, D.; Gera, I.; Eickholz, P. Influence of individual brightness and contrast adjustment on accuracy of radiographic measurements of infrabony defects. *Dentomaxillofac. Radiol.* **2011**, *40*, 177–183. [[CrossRef](#)]
10. Haralick, R.; Ramesh, V.; Hausmann, E.; Allen, K. Computerized detection of cemento-enamel junctions in digitized dental radiographs. In *The Images of the Twenty-First Century, Proceedings of the Annual International Engineering in Medicine and Biology Society, Seattle, WA, USA, 9–12 November 1989*; Institute of Electrical and Electronics Engineers (IEEE): Piscataway Township, NJ, USA, 2003.
11. Vasconcelos, K.D.F.; Evangelista, K.M.; Rodrigues, C.D.; Estrela, C.; De Sousa, T.O.; Silva, M.A.G. Detection of periodontal bone loss using cone beam CT and intraoral radiography. *Dentomaxillofac. Radiol.* **2012**, *41*, 64–69. [[CrossRef](#)]
12. Leung, C.C.; Palomo, L.; Griffith, R.; Hans, M.G. Accuracy and reliability of cone-beam computed tomography for measuring alveolar bone height and detecting bony dehiscences and fenestrations. *Am. J. Orthod. Dentofac. Orthop.* **2010**, *137*, S109–S119. [[CrossRef](#)]
13. Ludlow, J.B.; Davies-Ludlow, L.E.; Brooks, S.L.; Howerton, W.B. Dosimetry of 3 CBCT devices for oral and maxillofacial radiology: CB Mercuray, NewTom 3G and i-CAT. *Dentomaxillofac. Radiol.* **2014**. [[CrossRef](#)]
14. Chen, Y.-L.; Chang, H.-H.; Chiang, Y.-C.; Lin, C.-P. Application and development of ultrasonics in dentistry. *J. Formos. Med. Assoc.* **2013**, *112*, 659–665. [[CrossRef](#)]

15. Chifor, R.; Hedeşiu, M.; Bolfa, P.; Catoi, C.; Crişan, M.; Serbănescu, A.; Badea, A.F.; Moga, I.; Badea, M.E. The evaluation of 20 MHz ultrasonography, computed tomography scans as compared to direct microscopy for periodontal system assessment. *Med Ultrason.* **2011**, *13*, 120–126. [[PubMed](#)]
16. Chan, H.-L.; Sinjab, K.; Chung, M.-P.; Chiang, Y.-C.; Wang, H.-L.; Giannobile, W.V.; Kripfgans, O.D. Non-invasive evaluation of facial crestal bone with ultrasonography. *PLoS ONE* **2017**, *12*, e0171237. [[CrossRef](#)]
17. Nguyen, K.-C.T.; Le, L.H.; Kaipatur, N.R.; Zheng, R.; Lou, E.H.; Major, P.W. High-Resolution Ultrasonic Imaging of Dento-Periodontal Tissues Using a Multi-Element Phased Array System. *Ann. Biomed. Eng.* **2016**, *44*, 2874–2886. [[CrossRef](#)]
18. Nguyen, K.-C.T.; Le, L.H.; Kaipatur, N.R.; Major, P.W. Imaging the Cemento-Enamel Junction Using a 20-MHz Ultrasonic Transducer. *Ultrasound Med. Biol.* **2016**, *42*, 333–338. [[CrossRef](#)]
19. Nguyen, K.-C.T.; Pachêco-Pereira, C.; Kaipatur, N.R.; Cheung, J.; Major, P.W.; Le, L.H. Comparison of ultrasound imaging and cone-beam computed tomography for examination of the alveolar bone level: A systematic review. *PLoS ONE* **2018**, *13*, e0200596. [[CrossRef](#)]
20. Nguyen, K.-C.T.; Shi, D.; Kaipatur, N.R.; Lou, E.H.M.; Major, P.W.; Punithakumar, K.; Le, L.H. Graph Cuts-based Segmentation of Alveolar Bone in Ultrasound Imaging. In Proceedings of the 2018 IEEE International Conference on Bioinformatics and Biomedicine (BIBM), Madrid, Spain, 3–6 December 2018; pp. 2049–2055.
21. Nguyen, K.; Duong, D.; Almeida, F.; Major, P.; Kaipatur, N.; Pham, T.; Lou, E.; Noga, M.; Punithakumar, K.; Le, L. Alveolar Bone Segmentation in Intraoral Ultrasonographs with Machine Learning. *J. Dent. Res.* **2020**, *99*, 1054–1061. [[CrossRef](#)]
22. Tattan, M.; Sinjab, K.; Lee, E.; Arnett, M.; Oh, T.; Wang, H.; Chan, H.; Kripfgans, O.D. Ultrasonography for chairside evaluation of periodontal structures: A pilot study. *J. Periodontol.* **2020**, *91*, 890–899. [[CrossRef](#)] [[PubMed](#)]
23. Mathieu, V.; Anagnostou, F.; Soffer, E.; Haiat, G. Ultrasonic Evaluation of Dental Implant Biomechanical Stability: An In Vitro Study. *Ultrasound Med. Biol.* **2011**, *37*, 262–270. [[CrossRef](#)]
24. Sawant, A.R.; Zeman, H.D.; Muratore, D.M.; Samant, S.S.; Dibianca, F.A. Adaptive median filter algorithm to remove impulse noise in x-ray and CT images and speckle in ultrasound images. *Med. Imaging* **1999**, *3661*, 1263–1274. [[CrossRef](#)]
25. Jain, A.K. *Fundamentals of Digital Image Processing*; Prentice-Hall, Inc.: Hoboken, NJ, USA, 1989.
26. Solbo, S.; Eltoft, T. Homomorphic wavelet-based statistical despeckling of SAR images. *IEEE Trans. Geosci. Remote Sens.* **2004**, *42*, 711–721. [[CrossRef](#)]
27. Achim, A.; Bezerianos, A.; Tsakalides, P. Novel Bayesian multiscale method for speckle removal in medical ultrasound images. *IEEE Trans. Med. Imaging* **2001**, *20*, 772–783. [[CrossRef](#)]
28. Gonzalez, R.C.; Woods, R.E. *Digital Image Processing*; Prentice hall: Upper Saddle River, NJ, USA, 2002.
29. Arce, G.R. *Nonlinear Signal Processing: A Statistical Approach*; John Wiley & Sons: Hoboken, NJ, USA, 2005.
30. Khalid, M.; Pal, N.; Arora, K. Clustering of Image Data Using K-Means and Fuzzy K-Means. *Int. J. Adv. Comput. Sci. Appl.* **2014**, *5*, 160–163. [[CrossRef](#)]
31. Roa, I.; Del Sol, M.; Cuevas, J. Morphology of the Cement-Enamel Junction (CEJ), Clinical Correlations. *Int. J. Morphol.* **2013**, *31*, 894–898. [[CrossRef](#)]
32. Portney, L.G.; Watkins, M.P. *Foundations of Clinical Research: Applications to Practice*, 2nd ed.; Prentice Hall Health: Highland Park, NJ, USA, 2000.
33. Badersten, A.; Nilvéaus, R.; Egelberg, J. Reproducibility of probing attachment level measurements. *J. Clin. Periodontol.* **1984**, *11*, 475–485. [[CrossRef](#)]
34. Williamson, D.F.; Parker, R.A.; Kendrick, J.S. The Box Plot: A Simple Visual Method to Interpret Data. *Ann. Intern. Med.* **1989**, *110*, 916–921. [[CrossRef](#)]
35. Abolhassani, N.; Patel, R.; Moallem, M. Needle insertion into soft tissue: A survey. *Med. Eng. Phys.* **2007**, *29*, 413–431. [[CrossRef](#)]
36. Hacıhaliloglu, I.; Abugharbieh, R.; Hodgson, A.; Rohling, R. Bone Segmentation and Fracture Detection in Ultrasound Using 3D Local Phase Features. In *Medical Image Computing and Computer-Assisted Intervention—MICCAI 2008*; Metaxas, D., Axel, L., Fichtinger, G., Székely, G., Eds.; Springer: Berlin/Heidelberg, Germany, 2008; pp. 287–295.
37. Chifor, R.; Badea, M.E.; Mitrea, D.A.; Badea, I.C.; Crisan, M.; Chifor, I.; Avram, R. Computer-assisted identification of the gingival sulcus and periodontal epithelial junction on high-frequency ultrasound images. *Med. Ultrason.* **2015**, *17*, 273–279. [[CrossRef](#)]
38. Duong, D.Q.; Nguyen, K.-C.T.; Kaipatur, N.R.; Lou, E.H.M.; Noga, M.; Major, P.W.; Punithakumar, K.; Le, L.H. Fully Automated Segmentation of Alveolar Bone Using Deep Convolutional Neural Networks from Intraoral Ultrasound Images. In Proceedings of the 2019 41st Annual International Conference of the IEEE Engineering in Medicine and Biology Society (EMBC), Berlin, Germany, 23–27 July 2019; Volume 2019, pp. 6632–6635.
39. Abdolali, F.; Kapur, J.; Jaremko, J.L.; Noga, M.; Hareendranathan, A.R.; Punithakumar, K. Automated thyroid nodule detection from ultrasound imaging using deep convolutional neural networks. *Comput. Biol. Med.* **2020**, *122*, 103871. [[CrossRef](#)]
40. He, K.; Gkioxari, G.; Dollar, P.; Girshick, R.B. Mask R-CNN. In Proceedings of the IEEE International Conference on Computer Vision, Venice, Italy, 22–29 October 2017; pp. 22386–22397.